Numerical and experimental investigations into the rheological behaviour of wet foam flowing under a fence

Heni Dallagi, Fethi Aloui, Laurent Bouvier, Laurent Wauquier, Thierry Benezech

Title:

Numerical and experimental investigations into the rheological behaviour of wet foam flowing under a fence

List of authors and affiliations:

Heni Dallagi[1,2], Fethi Aloui[2], Laurent Bouvier[1], Laurent Wauquier[1], Thierry Benezech[1*]

[1]Univ. Lille, CNRS, INRAE, Centrale Lille, UMR 8207 - UMET - Unité Matériaux et Transformations, F-59000 Lille, France

[2]Polytechnic University Hauts-de-France, LAMIH CNRS UMR 8201, Campus Mont-Houy, F-59313 Valenciennes Cedex 9, France

Authors' email address:

heni.dallagi@inrae.fr

fethi.Aloui@uphf.fr

laurent.bouvier@inrae.fr

laurent.wauquier@inrae.fr

[*]Corresponding author:

thierry.benezech@inrae.fr

Postal address:

INRAE – PIHM UMET, Domaine du CERTIA 369 rue Jules-Guesde 59650 Villeneuve d'Ascq

1. Introduction

Foam is a two-phase gas-liquid fluid. It consists of gas dispersion in a continuous liquid phase containing surfactants. It presents, when considered from a physical process aspect relating to the mechanical evolution of its behaviour (Chen et al., 2020, 2019), various organizational scales (liquid-gas interfaces, wall liquid films, bubbles, plateau borders, capillarity phenomenon, etc.). However, the behaviour of this material varies far more than the fluids that compose it. It possesses both the mechanical properties of a solid and those of a liquid (AlQuaimi and Rossen, 2019; Blondin and Doubliez, 2002). The mechanical properties of foam (low density, high specific surface, disjoining pressure, foam-wall viscous friction) are sought in many industrial applications, from cosmetics to oil extraction, firefighting, mineral flotation and the cleaning of industrial equipment especially in agro-food industries (Al Saabi et al., 2021; Cappello et al., 2015; Schramm, 2000).

Static foam cleaning is widely used for open surfaces in food industries due to its interesting mechanical properties e.g. its generation of significant drag forces and the chemical properties of the surfactant as a cleaning agent (Mierzejewska et al., 2014). Recently it has been tested in closed system cleaning. When compared to the cleaning-in-place procedure in a linear pipe, foam flow cleaning showed higher efficiency for the removal of *Bacillus* spores from stainless steel surfaces (Al Saabi et al., 2021). However, preliminary data on the use of foam flow cleaning in complex situations such as cleaning over long distances or in the presence of singularities showed a decrease in the removal effectiveness (Al Saabi et al., 2020). The latter suggest that the change in foam proprieties after singularities was responsible for reducing the contamination removal efficiency. These can only be proven by a better knowledge of the foam structure, the understanding of its behavior in contact with a wall and also the modeling of the phenomena induced by its intrinsic rheological properties when flowing.

Most theoretical studies concerning foam properties are restricted to microscopic system analysis, such as the temporal evolution of its texture (bubble sizes and shapes) (Cantat, 2013; Farahmandfar et al., 2019) and its macroscopic properties, including its mechanical behaviour and its structure (bubbles trapped by different slipping films) (Panckow et al., 2021; Parikh et al., 2019). Foam under strong mechanical stresses behaves as a viscous liquid, while under low stresses it behaves like an elastic solid whose structure is deformed and returns to its initial state when constraint ceases. The common description of foam rheology suggests that for shear stresses lower than a yield stress of τ_0, the foam behaves as a solid, whereas for stresses exceeding the yield stress, the foam flows. Foam rheology has been studied to date

between these two physical characters (the linear elasticity as a solid and fluid behaviour), (Benzenine et al., 2010; Marchand et al., 2020). Given this complexity, several rheological studies have proposed a rheological model using a Power law (Firoze Akhtar et al., 2018), a Bingham model (Calvert and Nezhati, 1986), or a Hershel-Bulkley law (Marchand et al., 2020).

Flow around objects is a phenomenon that occurs frequently in practical life. Indeed, most transport systems in industrial facilities have various peculiarities, which cause major changes in the flow behaviour (Calvert, 1988; Deshpande and Barigou, 2001). Besides, flow under a fence has been studied in the contexts of loading on civil structures (Fang et al., 1999), solar collectors, the cooling of industrial machines and electronic components (Benzenine et al., 2010), particle transport (Dong et al., 2010), windbreak aerodynamics (Çoşkun et al., 2017), the design of nuclear reactors (Endres and Möller, 2001) and in that of heat exchangers (Cukurel et al., 2015; Tandiroglu, 2006). The optimization of industrial processes is closely related to the control of the systems' hydrodynamics. It should be noted that most studies carried out on the flow of a yield-stress fluid around obstacles propose experimental results interpreted on the basis of empirical or semi-empirical models (Badve and Barigou, 2020).

Foam flow through singularities has yet to be studied in depth, particularly in the case of fences. There is not enough information on the reorganization of a foam flow downstream of these singularities to fully understand the degradation of energy (Farahmandfar et al., 2019; Stevenson, 2012). A non-Newtonian rheological model had been proposed to model foam flow. As one might expect, the intensity of the effects induced by the presence of a fence, depends on the behaviour of the foam flow, the Reynolds number and the consequent flow regime conditions, the stress field and the flow morphology (Chovet et al., 2014; Dallagi et al., 2019, 2018).

Several experimental works have studied flowing foam in a horizontal square pipe with a built-in cross-section (Blondin and Doubliez, 2002; Tisné et al., 2003). These have shown that the flow arrangement, depending on the Reynolds number and foam quality, can vary from a plug-flow up to a complex regime affecting the liquid films along the surfaces and the foam itself, both in terms of velocity and of structure (bubble arrangement). This identification was confirmed by other studies (Aloui and Madani, 2008).

Given our current knowledge of foam flow behaviour, it would appear relevant to use CFD tools to describe this type of flow. Consequently, in a 2D simulation, using a non-Newtonian model with a yield shear stress τ_0, the Bingham law was used to model the plug foam flow at low velocities in a straight

channel with and without singularities (Chovet et al., 2014). However, this model only seemed to be adapted to plug flow regimes. However, in our previous numerical studies (Dallagi et al., 2018, 2019), CFD was successfully carried out using the Herschel-Bulkley law to describe the flow in a straight pipe or through half-sudden expansion.

This research investigates the flow characteristics of aqueous wet foam in a horizontal channel containing a fence, a relatively simple geometrical situation compared to the complexity encountered in agro-industrial equipment. The experimental part concerns the measurements of the pressure distribution, liquid film thicknesses, as well as the foam flow dynamics using PIV. The objective was to identify and model the foam structures and reorganization consequences both upstream and downstream of a fence, by selecting an adequate rheological model. Based on these models, 3D CFD numerical simulations were performed using the ANSYS CFX commercial code.

2. Materials and methods

2.1 Experimental device

Figure 1 (a) shows the experimental setup of the foam flow used in this study. This setup was designed to study horizontal foam flows in varying flow conditions both with and without a fence. The test pipe was 3.41 m long, with a 21 mm square cross-section. The fence was located 1.43 m downstream of the pipe inlet and was 10.5 mm high, and 5 mm wide, with a 45° angle evacuation. The coordinate system (Cartesian x, y, z) was located at the fence site at the channel bottom. The foam flow followed the x-axis as shown in Figure 1 (b). The flat surfaces of the duct allowed the easy implementation of the different measurement techniques for pressure outlets, particle image velocimetry (PIV) and conductometry.

The foams were generated by the injection of pressurized air through a permeable media (DURAN, pores size: 1 - 1.6 µm) into the generator container's water-surfactant solution. The role of the surfactant was to reduce the interfacial tension between gas and liquid in order to allow the formation of bubbles. The surfactant used in this experiment was sodium dodecyl sulfate (SDS) dissolved in osmosis water for 0.15% (w/w). The surface tension and the dynamic viscosity of this aqueous solution were respectively, 26.2 $mN.m^{-1}$ and 0.94 mPa.s.

Three different foam flow cases were generated (Case 1: foam at average velocity of 2 $cm.s^{-1}$, Case 2: foam at average velocity of 4 $cm.s^{-1}$, and Case 3: foam at average velocity of 6 $cm.s^{-1}$). These three flow regimes were obtained based on recommendations in previous works (Blondin and Doubliez, 2002; Ti□né et al., 2003). At Re of 32 (average velocity $\bar{u}$ of 2 $cm.s^{-1}$), the foam behaved as a plug flow, called a one-

dimensional regime. In this regime, the velocity vectors ($\vec{U}$) have a single uniform axial component in the flow direction ($\vec{U} = constant\ \overrightarrow{e_x}$). At Re of 65 (mean velocity of 4 cm.s^{-1}), the foam flow becomes faster at the bottom of the duct than at the top. The velocity vectors, in this case, have an axial component that depends solely on the vertical (y) coordinate ($\vec{U} = U\ (y)\ \overrightarrow{e_x}$). The third, a three-dimensional regime (Re = 97; $\bar{u}$ = 6 cm.s^{-1}) was a completely sheared foam flow, where the velocity vector has an axial component depending on both horizontal (z) and vertical (y) coordinates ($\vec{U} = U\ (y, z)\ \overrightarrow{e_x}$). These three conditions are summarized in Table 1.

A foam quality $\beta = \frac{Q_G}{Q_L + Q_G} = 65\%$ was chosen as corresponding to an aqueous wet foam, where Q_L and Q_G are designated as the volumetric flow rates (L.s^{-1}) of water and gas, respectively.

The Reynolds number of foam flow was calculated as:

$$Re = \frac{\rho_f . \bar{u} . d_h}{\mu_f} \quad (1)$$

where $\bar{u}$ is the average velocity, d_h is the hydraulic diameter (21 mm in this geometry cross-section). ρ_f is the foam density, based on the foam quality β (65%), liquid density ρ_L, and gas density ρ_G as:

$$\rho_f = (1 - \beta) . \rho_L + \beta . \rho_G \quad (2)$$

μ_f is the apparent viscosity of foam. This is determined from the viscosity of the liquid phase μ_L and the foam quality (Hatsehek, 1907). It should be noted that this calculated viscosity was used only to estimate the Reynolds number and does not imply a shear independent viscosity.

$$\mu_f = \frac{\mu_L}{1 - \beta^{1/3}} \quad (3)$$

2.2 Measurement techniques

To measure the static pressure along the channel, different pressure taps were used along the bottom wall and in the vertical symmetry plane of the channel. 23 pressure outlets were installed near the fence, eight of them being located upstream of the flow restriction mechanism and the other 15 downstream of it. The underlying liquid film located at the bottom of the channel ensured no bubbles flowed through the pressure measuring lines.

The velocity was measured using the Particle Image Velocimetry (PIV) technique and the method adopted for the foam flow was that described previously (Chovet et al., 2015). The PIV method is a non-intrusive optical technique, capable of measuring the displacement of particles in a laser light sheet. In foam flow, the gas/liquid interphase is darker than the rest of the flow (Chovet et al., 2015) and the contour of the bubble describes the whole flow movement (not the movement of each bubble), which obviates the use of

particles in tracking the flow. The flow is illuminated by a double-pulsed laser ND-YAG with 15 Hz of the "NEW WAVE" type, marketed by DANTEC. A synchronized CCD KODAK camera was installed with FLOWMAN software for the acquisition and processing. There is a 5% maximum error for the velocity measurements.

To determine the thickness of the liquid films at the pipe wall, the conductimetry method was used. This is an experimental technique based on the measurement of the impedance Z of the volume of liquid between the liquid-foam interface and two outcropping electrodes (powered by a generator that provides an alternative sinusoidal voltage) on the pipe wall as described previously (Tisné et al., 2004). In a square cross-section duct, the thickness of the liquid film between the foam and the walls increased from the top wall (few microns) to 2 mm at the bottom wall. The estimated error for the film thickness was of 8%.

2.3 Rheological model and numerical parameters

Simulations with the Eulerian-Eulerian multiphase models were made using ANSYS CFX® code. To simplify physical problems such as the interactions between bubbles and their slides over liquid films at the walls, the foam was defined as a pseudo-fluid, where its properties depend on those of the air and the water in laminar and isothermal conditions, as shown in the equations below. The underlying liquid film at the bottom of the channel was considered separately.

The ability of the proposed model to predict a wet foam behaviour in different cases of Reynolds numbers was ascertained by comparing the CFD results to the experimental data. Only the two extreme regimes observed in Case 1 and Case 3 were considered in this work.

Since the velocity conditions were quite low, the foam flow in this study can be considered as an instant laminar flux in isothermal conditions.

The following instantaneous equation of mass and momentum balances are presented as:

Mass balance:

$$\frac{\partial \rho}{\partial t} + \vec{\nabla}(\rho\, \vec{U}) = 0 \qquad (4)$$

where $\vec{U}$ is the velocity vector, ρ is the density and t is the time.

Momentum balance:

$$\rho \frac{\partial \vec{U}}{\partial t} = -\vec{\nabla} p + \vec{\nabla}(\bar{\bar{\tau}}) + \rho\, \vec{g} \qquad (5)$$

with p is the total static pressure, $\bar{\bar{\tau}}$ the stress tensor and $\rho\, \vec{g}$ the source term (volume forces).

where:

$$\bar{\bar{\tau}} = \bar{\bar{\tau_0}} + k(\dot{\gamma})^n \quad (6)$$

The foam is considered as a non-Newtonian pseudo-fluid with the yield shear stress (τ_0) described by the Herschel-Bulkley law as:

$$\begin{cases} \tau \leq \tau_0 \ ; \ \tau = \tau_0 \quad because\ \mu(\dot{\gamma}) \to \infty \\ \tau \geq \tau_0 \ ; \ \tau = \tau_0 + k\dot{\gamma}^n \end{cases} \quad (7)$$

Where $\dot{\gamma}$ is the shear rate, τ_0 is the yield stress, k, the consistency parameter, and n is the index of flow which depends on the specific mechanism of viscous dissipation through the flow. When n = 1, the Bingham law was applied. These parameters were identified experimentally and were adjusted numerically after validation by comparison of the results.

A consideration of the compressibility of the foam would not improve the precision of our numerical calculation. Indeed, according to Wood's law (equation 8, where the sound constant $k_s = 10$) (Pierre and Leroy, 2016), the sound velocity (v_s) in an aqueous foam is equal to 21 m.s^{-1}. Therefore, the Mach number (Ma) for all foam flow conditions is less than 0.3 (Ma=0.026, 0.055, and 0.058 for cases 1, 2, and 3 respectively).

$$v_s = \frac{k_s}{\sqrt{(\beta(1-\beta)}} \quad (8)$$

Unlike our previous simulations (Chovet et al., 2014; Dallagi et al., 2019, 2018), we considered the presence of the underlying liquid film developed at the bottom of the pipe for the two cases chosen. The thickness of this liquid film was around δ_{Bottom}=1.7 mm (Figure 1 (b)) (Aloui and Madani, 2007). Hence, two average foam velocity conditions were chosen: 2 and 6 cm.s^{-1} respectively inducing experimental 1D and 3D flow regimes. The other initial parameters relating to the water velocity U_{film} (Newtonian fluid) depend on the underlying film thickness, which can be defined as resembling a falling film with maximum velocity U_{max}. For the 1D flow regime U_{film} = 2 cm.s^{-1}. As for the case of high-velocity U_{max}=10 cm.s^{-1}, the foam was subjected to the stretching effect of the liquid film flowing at the bottom of the pipe at a higher velocity (Blondin and Doubliez, 2002; Tisné et al., 2004). The non-slipping conditions imposed zero velocities at the internal walls. The atmospheric pressure was defined as the output condition.

3. Results and discussions

3.1 Description of the foam flow

The evolution of the static pressure and the velocity profiles are the most important parameters when describing the rheological behaviour of the foam flow under the fence.

Figure 2 shows the longitudinal pressure gradient that was obtained from the static measurements of a series of pressure outlets along the channel (over 80 and 150 cm of length upstream and downstream of the fence respectively).

For both sides of the fence, both the pressure gradient and the velocity increased, so that the viscous dissipation close to the wall was greater in Case 3 than in Cases 1 and 2. Moreover, this gradient was higher upstream than downstream of the fence for the slowest foam (Cases 1 and 2). This could be directly related to the change in the foam's texture and structure, as a product of the bubble's reorganization and phase separation (forced gravitational drainage and coalescence). The same behaviour has been observed in other studies of foam flow under half-sudden expansion (Dallagi et al., 2019).

To better understand these observations, a study was carried of the velocity field over the lateral wall using the PIV system (Figure 3).

Plug flow was observed for Case 1. As the bubbles' velocities increased for Cases 2 and 3, the influence of the underlying liquid film was noted, as it seemed to pull the foam and deform it along the lateral and spanwise sides. Therefore, when approaching the fence, the foam flow became highly disturbed. First, under the contraction of the section, created by the fence, the static pressure increased, the foam slowed down and formed an aggregate of reduced-sized bubbles. Simultaneously, the fence created the first obstacle for bubbles, thereby generating a "stagnant" cover, altering the velocity of other bubbles passing through the fence. Then, when passing under the fence (x = 0 mm), the foam opposed the compression of the bubbles and accelerated brusquely and reached its maximum axial velocity (4.3, 9, and 14 cm.s^{-1} for Cases 1, 2, and 3 respectively). Downstream, when the foam came out of this acceleration forced by the obstacle, a second smaller stagnant area was generated at the top of the duct near the obstacle.

In addition, an asymmetry was observed between the vertical velocity fields upstream and downstream of the fence (maximum 47, 38, and 29% for Cases 1, 2, and 3 respectively). At greater distances from the fence, whether upstream or downstream (for x > -25 mm and x > 25 mm), the vertical velocities fell to zero and the foam flow only reacted axially. Therefore, three transition states of behaviour were observed; deceleration, acceleration, and stabilization. At a distance of x > -25 mm, the foam began to

resist the section reduction. The deceleration was greatest at x = -5 mm (-0.8, -1.8, -3.6 cm.s^{-1} for Cases 1,2 and 3 respectively). However, the foam passing under the fence (at $0 < x \leq 5$ mm) and therefore subjected to compression shown just after the fence a clear acceleration. The vertical velocity profile became parabolic and attained its highest speed (1.5, 2.6, and 3.8 cm.s^{-1} for Cases 1, 2, and 3 respectively). Then, at x = 25 mm the foam flow developed fully and gradually slowed down to return to its initial state for the rest of the channel.

The flow behaviour of the foam is thus clearly described here. When passing through a fence, an increase in stress occurs, where the foam yield passes the threshold and flows as a viscoelastic fluid. Visibly, even though the velocity field seems to be identical to that upstream side when distant from the fence, a reorganization of the foam ensues whereby the foam texture and granulometry change to present a coalescence phenomenon (shown in the Supplementary Data 1, for Case 1).

The change of the pipe section leads to a change in the foam structure and texture. Indeed, under the decrease of the pressure induced by the section reduction, foam bubbles are distorted, and the inter-bubble liquid film varies. This deformation induces an increase in the surface energy of the bubbles that consequently store elastic energy in proportion to the surface tension (Dollet and Raufaste, 2014; Höhler and Cohen-Addad, 2005). The foam reveals its elastic character (Gorlier et al., 2017) as the low density and the high active surface push the bubbles up into the channel to fill the entire height of the duct's cross-section, to return to its initial equilibrium. The elastic modulus $G = 0.5\ \frac{\gamma}{R}$ for the three cases is 13, 29, and 29.5 Pa for the 1D, 2D, and 3D regimes respectively. γ and R are the surface tension and the bubble radius, respectively (Gorlier et al., 2017).

In this case, the foam became wetter at the bottom of the duct due to gravitational drainage followed by an increase in the size of the bubbles in the upper part, ensuing from various phenomena such as the coalescence and expansion of the bubbles. The consequence of this phenomenon is the non-uniformity of both heat and mass transfers along the duct and of the wall shear stress.

The analysis of the bubble size shows a change in the foam structure after the fence. Figure 4 (a) presents an example of the bubble size distribution for a section of 2 cm^2 just upstream and downstream of the fence for Case 1, fitted by a lognormal model. PIV images were taken and treated with Piximètre 1.5 software. These results confirmed the change in the foam texture after the fence previously observed (Aloui and Madani, 2007). As seen in cumulative probability, the bubbles downstream of the fence were

20% larger than upstream, as a consequence of the various factors associated with the fence and the coalescence of the bubbles.

The evolution of the global and local void fraction can be deduced, with the global fraction remaining almost unchanged the same and the local void increasing as it approaches the top of the duct, where the largest bubbles are located after the fence. Such phenomena would be related both to the variation of the pressure, gas density and the temperature, the two later which in turn are governed by the heat exchange between the gas and the liquid phases.

3.2 Rheological model

Foam flow presents complex properties that make it difficult to define the wall shear rate and the velocity gradient (opacity, reflections, small scales, etc.). One way to obtain this is to assume that the velocity gradient is equal to the bubble's velocity over the wall of the channel, in relation to the thickness of the liquid slip layer (e) at the top side of the duct (Blondin and Doubliez, 2002):

$$\dot{\gamma}_w = \frac{\partial u}{\partial y} \tag{9}$$

The average slip layer thickness was measured by the conductometry method at the top of the channel (30, 26, and 33 µm for Cases 1, 2, and 3 respectively). Supplementary Data 2 (conductometry signal over the top wall for Cases 1, 2, and 3) represents a typical signal delivered at the top of the wall for the three cases).

The mean wall shear stress can be computed as:

$$\bar{\tau}_w = \frac{\Delta P}{\Delta x}\frac{d_h}{4} \tag{10}$$

where $\frac{\Delta P}{\Delta x}$ is the pressure gradient and $d_h (= 21mm)$ is the hydraulic diameter.

Several methods exist for measuring the yield stress developed for non-Newtonian fluids such as stress relaxation, stress ramping, frequency sweeping and viscometry. These techniques are applied for static foam conditions and present a great uncertainty due to foam instability issues, such as degradation, expansion, and the absence of wall slip (Khan and Armstrong, 1987; Sullivan and Yee, 1984).

Determining the flow curve of the foam can be the most appropriate way to identify the rheological behaviour of this fluid complex under dynamic conditions (Sherif et al., 2015). Figure 5 describes the change in the shear stress as a function of the shear rate for the three cases studied.

The flow curve of the foam obtained exhibits a strong non-Newtonian fluid behaviour, with a threshold stress ($\tau(\dot{\gamma} = 0) \neq 0$), whose apparent viscosity is highly sensitive to the shear rate change. This can be

attributed to the development of the foam structure discussed above. This behaviour best matches the Herschel-Bulkley rheological model.

The flow behaviour index n can be determined from the slope of Log $(\tau_w - \tau_{w\,\dot{\gamma}_w \to 0})$ versus Log $(\dot{\gamma}_w)$ plot (Equation 11). For our case, the foam presented as a shear-thinning fluid.

$$n = \frac{d\left(ln\left(\tau_w - \tau_{w\,\dot{\gamma}_w \to 0}\right)\right)}{d\,(ln\,(\dot{\gamma}_w))} \tag{11}$$

The method used is based on the Rabinowitsch-Mooney equation, which provides the wall shear rate for non-Newtonian flow (Firoze Akhtar et al., 2018). This is presented elsewhere (Khan and Armstrong, 1987).

Modeling foam flows experimentally is a challenge, given the complexity of the foam structure, the experimental artefacts, and the possibility of error presented by the different measurement methods used.

A numerical simulation can be a solution to adjust the parameters of the rheological model identified experimentally.

Table 2 shows the rheological parameters identified that describe the Hershel-Bulkley model and the Bingham model proposed in previous work (Chovet et al., 2014). The density of air and water fluids are respectively taken as being 1.21 and 1003 kg.m^{-3}.

However, this rheological model also has its limits, as it is sensitive to the choice of parameters which change with the geometry and the foam quality (Dallagi et al., 2018; Marchand et al., 2020). The numerical identification of these parameters was chosen after the experimental identification discussed before. It then was adjusted based on the inverse simulation: starting with known experimental results, setting the parameters, and checking the velocity and pressure profiles obtained, then comparing these to the experimental ones. Validations of these results are always mandatory to ensure their relevance to experiments (results will be discussed below and display close agreement). The second instrument for adjusting this parameter is the CFD convergence, which minimizes the residue calculation. Indeed, this model presents a severe discontinuity in its rheological behaviour due to the threshold yield stress and the index number. It also induces some numerical difficulties in the convergence if the parameters imposed are not coherent with the boundary conditions (Messelmi, 2019). This problem has been the subject of other studies aiming to regularize the discontinuity of the exact visco-plastic behaviour, in order to allow its implementation in standard numerical solvers (Liu et al., 2002; Moreno et al., 2016).

Accepting these limits of experimental uncertainty, a lack of wall slip and numerical convergence, the Herschel-Bulkley model seems to fit the experimental observations more closely at low shear stress, with

a slight deviation under higher conditions. In contrast, the Bingham model proposed previously by (Chovet et al., 2014) fails to support the experimental data shown in Table 2.

The numerical results for the two rheological models (Bingham and Hershel-Bulkley) presented in Table 2, will be compared below with experimental ones for Cases 1 and 3.

3.3 Case of Foam Flow (plug flow) at low velocity (*Re*=32)

3.3.1 Longitudinal pressure distribution

To validate the CFD numerical calculations, it is necessary to examine whether the pressure distribution generated by the Herschel-Bulkley model confirms the experimental results. Figure 6 shows the longitudinal static pressure losses ΔP inside each cross-section of the horizontal duct including the fence at its centre.

As illustrated in Figure 6 (a), when distant from the fence, whether upstream or downstream, we respectively have an establishment and a re-establishment of the foam flow regime. Results show a linear decrease in the static pressure upstream and downstream of the fence. The transition through the fence is followed by a slight disturbance in the pressure drop with the same energy degradation on both sides of the fence. This similarity can result in a similar pressure gradient value upstream and downstream of the fence, where both curves have almost the same slope (-615 $Pa.m^{-1}$ for the upstream and -745 $Pa.m^{-1}$ for the downstream). The presence of the fence in the pipe represents a disruption for the foam flow. Its influence extends upstream as well as downstream of the fence. Indeed, according to the magnification in Figure 6, the change in the flow starts approximately from the x = -260 mm ($\simeq$-12.4d_h) until x = 220 mm ($\simeq$10.5d_h).

CFD simulations and experimental measurements present the same evolution with a maximum deviation close to 5% near the fence. This comparison allows a validation of the chosen boundary conditions adopted i.e. the rheology model used, and the parameters fixed for the simulation.

3.3.2 Singular pressure drop

According to (Aloui and Madani, 2008, 2007), the singular pressure drop caused by the fence and the global wall friction against the wall in the vicinity of the fence can be written as:

$$\Delta P_{Singular} = P_2(x = 0^+)_{downstream} - P_1(x = 0^-)_{upstream} \quad (18)$$

$$\Delta P_{friction} = \Delta P_{tot} - \Delta P_{singular} \quad (19)$$

where $\Delta P_{singular} = \frac{1}{2}.\xi.\rho_f.U^2$ can be considered as the singular pressure due to the kinetic effects of the fence. The singular pressure drop coefficient (ξ) is equal to 8.52 (Aloui and Madani, 2008), and P_1 and P_2 are the pressure in the upstream and downstream of the fence respectively.

In the case of Re = 32, and for a foam quality of 65%, the singular pressure drop was estimated *as* $\Delta P_{singular} \simeq$ 58 Pa (determined by extrapolating the regular pressure evolution downstream and upstream of the fence as shown in Figure 6 (b)). This numerical result has a slightly larger value than the experimental one (≃40 Pa). This means that the foam flow adapts faster than the Herschel-Bulkley fluid to the section change and its behaviour is less affected by the fence. Besides, the results obtained show that foam flow under a fence is the exact opposite of the flow of a Newtonian liquid single-phase. The contribution of the pressure loss by friction in the global singular pressure drop is about 98%. This means that the energy loss in this condition of foam flow under the fence is not dominated by any kinetic effects of the fence ($\Delta P_{singular}$=1.15 Pa), but by the friction near the fence ($\Delta P_{friction} \simeq$ 57 Pa).

3.3.3 Local averaged velocity fields

To determine the behaviour of Herschel-Bulkley fluid under the fence, it appears necessary to visualize the velocity fields and the deformation of their profiles, by giving a comparison of the numerical simulation results with the experimental ones. Figure 7 represents an example of a velocity field for the numerical simulations of the CFD Herschel-Bulkley fluid.

The presence of the fence disrupts the flow by forcing the foam to bypass it, inducing the creation of stagnant areas around the fence (absence of velocity vectors on both sides in the vicinity of the fence as shown in Figure 7 (a)). The visualization of the velocity field through the horizontal plane at y =19 mm (Figure 7 (b)), confirms the direction of the flow. Thus, the upstream dead zone is longer than that one downstream ($l_1 > l_2$, where l_1 ($\simeq 0.47 d_h$) and l_2 ($\simeq 0.23 d_h$) are respectively the lengths of the appearance of dead zones immediately upstream and downstream of the fence).

The comparison between these numerical and experimental results shows a close concordance (Supplementary data. 3 (Averaged u-axial component (a) and v-vertical component velocity field (b) of experimental foam flow and the Herschel-Bulkley model under the fence).

The effect of the fence can be quantified by plotting the evolution of the axial and vertical components' velocity profiles along the x-coordinate near the fence for different positions upstream and downstream of the fence (Figure 8). These velocity profiles allow a better comparison between the foam flow, the

Bingham model proposed by (Chovet et al., 2014) and our proposed model, namely the Herschel-Bulkley law.

A close similarity between the experimental and the CFD results were thus observed with the Herschel-Bulkley CFD model results showing less deviation than the Bingham model ones.

As mentioned above, simulating a complex fluid such as foam is a challenge because of the presence of several phenomena. For instance, it is difficult for the software code to reproduce incidents such as the slip and deformation of bubbles, coalescence, and foam drainage (Golemanov et al., 2008). The Herschel-Bulkley model, based on the hypothesis of a pseudo-fluid, can describe the behaviour of the foam flow more reasonably than the Bingham model. Hence, Axial velocity component results by the Bingham model show a discrepancy of between 21% and 37% between the foam flow experiments and the CFD simulations, while Herschel-Bulkley only shows a difference of 8% to 21%. For both models, vertical velocity component profiles show the greatest deviation, where the foam deformation increases near the fence (at x=-5mm), entailing its maximum deviation of 50%. It should be noted that contrary to CFD results, the experimental data indicate a slip at the walls. While accepting its limits, this study has shown that the rheological Herschel-Bulkley fluid model is capable of satisfactorily describing the behaviour of flowing foams under a fence.

Supplementary Data 4 illustrates the velocity profiles on the upper part in three planes along x-z axes: at the top of the channel (y = 19 mm), in the middle (y = 10.5 mm), and at the bottom (contact with the underlying liquid film, for y = 2mm). This was achieved by numerical simulations to define and to present the evolution in foam flow's behaviour along the x-coordinate near the fence at different locations. It should be noted that the experimental results did not investigate the velocity fields inside the foam and far from walls, as the opacity of the foam limited the PIV technique's capacity to visualize the flow. In such cases, CFD studies are of distinct benefit.

It is clear, that the foam flow behaves like plug flow, hence as a unidirectional regime. Therefore, these results confirm the presence of dead areas at the top of the channel (at y = 19 mm and -15 mm < x < 15 mm), where the velocity is nil and that the maximum acceleration occurs at the location of the fence when x = 0 mm and y = 10.5 mm.

3.3.4 Underlying film thickness in the vicinity of the fence

Wet foam flows also create liquid films along the bottom surface of the duct. This thickness can affect the dynamic behaviour of the flow. Previous works have also shown that the thickest liquid film is formed at the bottom of a channel arranged horizontally under the gravitational force effects and more specifically under the foam drainage (drainage of the liquid through the plateau borders or bubbles' contours) (Tisné et al., 2004).

Despite the experimental data available, the model was not able to accurately reproduce this phenomenon. This is the reason why a liquid (water) film was imposed at the bottom channel as a second inlet condition, unlike previous attempts to model the foam flow using CFD tools (Chovet et al., 2014). Figure 9 (a) presents the velocity evolution of the underlying liquid film. We noted that the velocity of the liquid film increased when approaching the fence to reach a maximum value caused by the narrowing of the section (velocity of 3.3 $cm.s^{-1}$ at x = 0 mm). After the fence, the velocity of the film liquid increased gradually to recover its initial value of 2.1 $cm.s^{-1}$.

To better understand the deviations and the disturbance caused by the fence, Figure 9 (b) represents the thickness evolution of the underlying liquid layer. The underlying liquid film thickness remained constant and had no pronounced fluctuations upstream or downstream of the fence. It was stable and its thickness was about 1.9 mm. However, this thickness gradually decreased below the fence and reached its minimum value, which was about 0.9 mm. This modification was mainly due to the abrupt acceleration of the outgoing flow through the reduced cross-section passage, which then exerted compression on the underlying liquid film.

This evolution studied by CFD is only an approximation of the underlying liquid film thickness. However, it does present a discrepancy of about 45% from the experimental results given by the conductimetric method. These show the same evolution except that the liquid film is 20% thicker downstream than upstream of the fence. This thickness difference is mainly due to the foam drainage phenomenon, which increased with the acceleration of the foam flow and after the reorganization of the bubbles (Golemanov et al., 2008; Marchand et al., 2020). The experimental results again indicate that the fence induced some changes in the foam flow structure.

3.4 Case of foam flow at higher velocity (*Re* = 97)

The main goal was to test the ability of the rheological model proposed to reproduce the physical phenomena response of high Reynolds numbers, where the yield shear stress is exceeded. Figure 10 illustrates the evolution of axial and vertical velocity components along the x and y coordinates at different distances from the fence.

The validation of the CFD results is based on the experimental measurements provided by the PIV technique, in order to investigate the foam flow velocity components' profiles under the same conditions.

The comparison between experimental and numerical results shows an agreement, despite the observed deviations for the Herschel-Bulkley model (from 19% to 47% for the axial velocity component and from 30% to 74% for the vertical velocity component). On the other hand, it shows to what extent the Bingham model describes the sheared condition of the foam flow (from 30% to 100% difference for the axial and vertical velocity components). The greatest deviation that occurred for the vertical velocity component profiles is at x=-5mm. This difference is partly due to the use of a laminar regime instead of the turbulent regime, causing the underlying liquid layer to slide and secondly, due to the compressibility of the foam gas phase (experimental fluid) and to its resistance to the narrowing of the duct cross-section, thereby generating a viscoelastic response by the foam.

The Herschel-Bulkley model proposed is written as the sum of a yield stress τ_0 and a viscous stress τ_v. First, as discussed above, the experimental identification of the threshold stress under dynamic conditions is a challenge due to experimental artefacts. On the other hand, the capillary pressure of the bubbles, the adsorption of the surfactant layer on the surfaces of the bubbles and the viscous friction between the bubbles and the wetting walls provide a scale for the viscous stress (Borkowski et al., 2020; Denkov et al., 2005). As the foam in this work is identified as a pseudo-fluid which does not reflect the real identity of the foams i.e. a dispersion of gas bubbles in liquids containing surfactants according to (Langevin, 2017), it is difficult for Herschel-Bulkley to represent these phenomena and accurately reproduce the experimental behaviour of high-velocity foam flow. Thus, according to several previous studies (Messelmi, 2019; Moreno et al., 2016), some limitations of this model should be studied and experiments performed in future works using a slip wall condition, in order to focus on a simulation of the shape, trajectory, and interaction of bubbles on the walls (Ge and Liu, 2021).

Concerning the foam flow behaviour on the spanwise plane, the velocity fields are not accessible experimentally using the PIV technique because of the opacity of the foam, as already mentioned. Figure

11 shows the evolution of the velocity profiles thanks to CFD, along the z-coordinate near the fence, plotted in three horizontal planes: at the bottom of the channel (x, y = 2 mm, z), in the middle (x, y = 10.5 mm, z), and at the top (x, y = 19 mm, z).

In contrast to the first case (Re = 32), the shear stress in the channel far exceeds the yield stress inducing velocity profiles with parabolic shapes of the as shown in Figures 11 (a), and 11 (b). In addition, there is a great contrast comparing the foam velocities at the top (low velocities) and at the bottom (high velocities) of the channel.

4. Conclusions

In this work, the effect of the fence both on the characteristics of the foam flow, as well as on the different phenomena observed, has been studied using both experimental and CFD simulation approaches, giving original results.

Different measurements were made including liquid film thickness, foam structure and its flow behaviour. This allowed us to clearly understand the deformation of the foam in the vicinity of the fence, where it displays marked elasticity.

CFD results were directly compared to those obtained experimentally under the same flow conditions.

Attention was focused on the velocity component profile evolution upstream and downstream of the fence. The CFD simulations and the experimental results showed the same trends. The Herschel-Bulkley rheological model can better describe the foam flow for all regimes (3 cases studied), than the Bingham rheological model. As for the lower Reynolds number, the two fluids behave like a plug-type flow presenting a mean deviation of 15%. In contrast, in the case of higher Reynolds number (Case 3), some greater deviations appear near to the fence, which can reach more than 50% with Hershel-Bulkley and be completely different for Bingham. This considerable discrepancy reflects the higher sensitivity of the chosen model (pseudo-fluid flow) and its limits in presenting this type of foam flow deformation and the bubbles' reorganization. This is probably related to the actual rheological properties of the foam modelled here by a quite simple Herschel-Bulkley pseudo-fluid model. However, some likely important phenomena should be taken into account in the future such as the compressibility of the foam gas phase and the slipping of the foam bubbles on the channel walls (phenomena existing at the bubble-bubble and bubble-liquid film interfaces) highlighted by the different experimental methods.

Despite the complexity of the proprieties involved in the physics of foams (border stability plateau, effect of surface tension, drainage of liquid, bubble movements, coarsening, ripening, coalescence,

compressibility), the non-Newtonian fluid model with threshold stress gives a quite good approximation of the foam's flow behaviour and its deformation on encountering a fence.

In a previous work, we have demonstrated that compared to the standard cleaning-in-place, the use of foam flow to remove bacterial contamination (spores and biofilms) can improve the cleaning efficiency and dramatically reduce the consumption of water and energy (Al Saabi et al., 2021). However, this enhancement of cleaning was closely related to the foam proprieties such as void fraction, shear stress, liquid film thickness, bubble size, and its stabilities (Schad et al., 2021). Modification of the ducts geometries and the presence of specific equipment (valves, fences in heat exchangers, corners or other obstacles) in agro-food processing industries would thus significantly change the foam structure and the flow organization and eventually, reduce the efficiency of foam cleaning (Al Saabi et al., 2020). Computational Fluid Dynamic approaches in a first step assist in identifying the temporal evolution of the flow parameters in complicated situations where experimental definition is difficult. Consequently, their use helps to improve cleaning efficiency when modeling and designing industrial equipment and installing its accessories, thereby ensuring high foam stability and a fast recovery of the flow regime due to a better flow organization. Further studies could investigate the impact of such singularities on the removal kinetics of static bacterial biofilms under foam flow cleaning regimes.

Acknowledgment

This work was supported by the National Institute for Agricultural Research INRAE (Villeneuve d'Ascq, France, laboratory UMET UMR 8207) and the LAMIH CNRS UMR 8201 (Université Polytechnique Hauts-de-France, INSA Hauts-de-France, France). The authors wish to express their gratitude to the Interreg V, GoToS3, Vegitec project (EU) and to the Erflow-Engineering (Nantes, France) for the support and funding provided for this research.

REFERENCES

Al Saabi, A., Dallagi, H., Aloui, F., Faille, C., Rauwel, G., Wauquier, L., Bouvier, L., Bénézech, T., 2021. Removal of Bacillus spores from stainless steel pipes by flow foam: Effect of the foam quality and velocity. J. Food Eng. 289, 110273. https://doi.org/10.1016/j.jfoodeng.2020.110273

Al Saabi, A.-A., Benezech, T., Faille, C., Aloui, F., Rauwel, G., 2020. Foam flow for cleaning of closed equipment contaminated by Bacillus cereus spores or Pseudomonas fluorescens biofilms. Lille, France.

Aloui, F., Madani, S., 2008. Experimental investigation of a wet foam flow through a horizontal sudden expansion. Exp. Therm. Fluid Sci. 32, 905–926. https://doi.org/10.1016/j.expthermflusci.2007.11.013

Aloui, F., Madani, S., 2007. Wet foam flow under a fence located in the middle of a horizontal duct of square section. Colloids Surf. Physicochem. Eng. Asp. 309, 71–86. https://doi.org/10.1016/j.colsurfa.2007.01.009

AlQuaimi, B.I., Rossen, W.R., 2019. Characterizing foam flow in fractures for enhanced oil recovery. J. Pet. Sci. Eng. 175, 1160–1168. https://doi.org/10.1016/j.petrol.2018.06.020

Badve, M., Barigou, M., 2020. Local description of foam flow, deformation and pressure drop in narrow constricted channels. Int. J. Multiph. Flow 103279. https://doi.org/10.1016/j.ijmultiphaseflow.2020.103279

Benzenine, H., Saim, R., Abboudi, S., Imine, O., 2010. Numerical simulation of the dynamic turbulent flow field through a channel provided with baffles: comparative study between two models of baffles: transverse plane and trapezoidal 14.

Blondin, E., Doubliez, L., 2002. Particle imaging velocimetry of a wet aqueous foam with an underlying liquid film. Exp. Fluids 32, 294–301. https://doi.org/10.1007/s003480100318

Borkowski, M., Kosior, D., Zawala, J., 2020. Effect of initial adsorption coverage and dynamic adsorption layer formation at bubble surface in stability of single foam films. Colloids Surf. Physicochem. Eng. Asp. 589, 124446. https://doi.org/10.1016/j.colsurfa.2020.124446

Calvert, J.R., 1988. The flow of foam through constrictions. Int. J. Heat Fluid Flow 9, 69–73. https://doi.org/10.1016/0142-727X(88)90032-X

Calvert, J.R., Nezhati, K., 1986. A rheological model for a liquid-gas foam. Int. J. Heat Fluid Flow 7, 164–168. https://doi.org/10.1016/0142-727X(86)90016-0

Cantat, I., 2013. Liquid meniscus friction on a wet plate: Bubbles, lamellae, and foams. Phys. Fluids 25, 031303. https://doi.org/10.1063/1.4793544

Cappello, J., Sauret, A., Boulogne, F., Dressaire, E., Stone, H.A., 2015. Damping of liquid sloshing by foams: from everyday observations to liquid transport. J. Vis. 18, 269–271. https://doi.org/10.1007/s12650-014-0250-1

Chen, L., Huang, M., Li, Z., Liu, D., Li, B., 2020. Experimental study on the characteristics of foam flow in fractures. J. Pet. Sci. Eng. 185, 106663. https://doi.org/10.1016/j.petrol.2019.106663

Chen, S., Liu, H., Yang, J., Zhou, Y., Zhang, J., 2019. Bulk foam stability and rheological behavior of aqueous foams prepared by clay particles and alpha olefin sulfonate. J. Mol. Liq. 291, 111250. https://doi.org/10.1016/j.molliq.2019.111250

Chovet, R., Aloui, F., Keirsbulck, L., 2015. Wall Shear Stress Generated by Aqueous Flowing Foam, in: Volume 1: Symposia. Presented at the ASME/JSME/KSME 2015 Joint Fluids Engineering Conference, American Society of Mechanical Engineers, Seoul, South Korea, p. V001T14A001. https://doi.org/10.1115/AJKFluids2015-14039

Chovet, R., Aloui, F., Keirsbulck, L., 2014. Gas-Liquid Foam Through Straight Ducts and Singularities: CFD Simulations and Experiments, in: Volume 1B, Symposia: Fluid Machinery; Fluid-Structure Interaction and Flow-Induced Noise in Industrial Applications; Flow Applications in Aerospace; Flow Manipulation and Active Control: Theory, Experiments and Implementation; Multiscale Methods for Multiphase Flow; Noninvasive Measurements in Single and Multiphase Flows. Presented at the ASME 2014 4th Joint US-European Fluids Engineering Division Summer Meeting collocated with the ASME 2014 12th International Conference on Nanochannels, Microchannels, and Minichannels, American Society of Mechanical Engineers, Chicago, Illinois, USA, p. V01BT14A003. https://doi.org/10.1115/FEDSM2014-21190

Çoşkun, Ş., Hazaveh, H.A., Uzol, O., Kurç, Ö., 2017. Experimental investigation of wake flow field and wind comfort characteristics of fractal wind fences. J. Wind Eng. Ind. Aerodyn. 168, 32–47. https://doi.org/10.1016/j.jweia.2017.05.001

Cukurel, B., Selcan, C., Stratmann, M., 2015. Convective heat transfer investigation of acoustically excited flow over an isolated rib obstacle. Int. J. Heat Mass Transf. 91, 848–860. https://doi.org/10.1016/j.ijheatmasstransfer.2015.07.043

Dallagi, H., Al Saabi, A., Faille, C., Benezech, T., Augustin, W., Aloui, F., 2019. CFD Simulations of the Rheological Behavior of Aqueous Foam Flow Through a Half-Sudden Expansion, in: Volume 1: Fluid Mechanics. Presented at the ASME-JSME-KSME 2019 8th Joint Fluids Engineering Conference, American Society of Mechanical Engineers, San Francisco, California, USA, p. V001T01A030. https://doi.org/10.1115/AJKFluids2019-4650

Dallagi, H., Gheith, R., Al Saabi, A., Faille, C., Augustin, W., Benezech, T., Aloui, F., 2018. CFD Characterization of a Wet Foam Flow Rheological Behavior, in: Volume 3: Fluid Machinery; Erosion, Slurry, Sedimentation; Experimental, Multiscale, and Numerical Methods for Multiphase Flows; Gas-Liquid, Gas-Solid, and Liquid-Solid Flows; Performance of Multiphase Flow Systems; Micro/Nano-Fluidics. Presented at the ASME 2018 5th Joint US-European Fluids Engineering Division Summer Meeting, American Society of Mechanical Engineers, Montreal, Quebec, Canada, p. V003T20A004. https://doi.org/10.1115/FEDSM2018-83338

Denkov, N.D., Subramanian, V., Gurovich, D., Lips, A., 2005. Wall slip and viscous dissipation in sheared foams: Effect of surface mobility. Colloids Surf. Physicochem. Eng. Asp. 263, 129–145. https://doi.org/10.1016/j.colsurfa.2005.02.038

Deshpande, N.S., Barigou, M., 2001. The fow of gas-liquid foams through pipe fttings 8.

Dollet, B., Raufaste, C., 2014. Rheology of aqueous foams. Comptes Rendus Phys. 15, 731–747. https://doi.org/10.1016/j.crhy.2014.09.008

Dong, Z., Luo, W., Qian, G., Lu, P., Wang, H., 2010. A wind tunnel simulation of the turbulence fields behind upright porous wind fences. J. Arid Environ. 74, 193–207. https://doi.org/10.1016/j.jaridenv.2009.03.015

Endres, L.A.M., Möller, S.V., 2001. On the fluctuating wall pressure field in tube banks. Nucl. Eng. Des. 203, 13–26. https://doi.org/10.1016/S0029-5493(00)00293-4

Fang, F., Ueng, J., Liu, C., Soong, P., 1999. Dynamic response of an elastic fence under wind action. J. Chin. Inst. Eng. 22, 469–478. https://doi.org/10.1080/02533839.1999.9670485

Farahmandfar, R., Asnaashari, M., Taheri, A., Rad, T.K., 2019. Flow behavior, viscoelastic, textural and foaming characterization of whipped cream: Influence of Lallemantia royleana seed, Salvia macrosiphon seed and carrageenan gums. Int. J. Biol. Macromol. 121, 609–615. https://doi.org/10.1016/j.ijbiomac.2018.09.163

Firoze Akhtar, T., Ahmed, R., Elgaddafi, R., Shah, S., Amani, M., 2018. Rheological behavior of aqueous foams at high pressure. J. Pet. Sci. Eng. 162, 214–224. https://doi.org/10.1016/j.petrol.2017.12.050

Ge, Y., Liu, T., 2021. Numerical simulation on bubble wall shape evolution and uniformity in poly(ethylene terephthalate) foaming process. Chem. Eng. Sci. 230, 116213. https://doi.org/10.1016/j.ces.2020.116213

Golemanov, K., Tcholakova, S., Denkov, N.D., Ananthapadmanabhan, K.P., Lips, A., 2008. Breakup of bubbles and drops in steadily sheared foams and concentrated emulsions. Phys. Rev. E 78, 051405. https://doi.org/10.1103/PhysRevE.78.051405

Gorlier, F., Khidas, Y., Pitois, O., 2017. Coupled elasticity in soft solid foams. J. Colloid Interface Sci. 501, 103–111. https://doi.org/10.1016/j.jcis.2017.04.033

Hatsehek, V.E., 1907. Die Viskositiit der Dispersoide. 6.

Höhler, R., Cohen-Addad, S., 2005. Rheology of liquid foam. J. Phys. Condens. Matter 17, R1041–R1069. https://doi.org/10.1088/0953-8984/17/41/R01

Khan, S.A., Armstrong, R.C., 1987. Rheology of foams: II. Effects of polydispersity and liquid viscosity for foams having gas fraction approaching unity. J. Non-Newton. Fluid Mech. 25, 61–92. https://doi.org/10.1016/0377-0257(87)85013-9

Langevin, D., 2017. Aqueous foams and foam films stabilised by surfactants. Gravity-free studies. Comptes Rendus Mécanique 345, 47–55. https://doi.org/10.1016/j.crme.2016.10.009

Liu, B.T., Muller, S.J., Denn, M.M., 2002. Convergence of a regularization method for creeping flow of a Bingham material about a rigid sphere. J. Non-Newton. Fluid Mech. 102, 179–191. https://doi.org/10.1016/S0377-0257(01)00177-X

Marchand, M., Restagno, F., Rio, E., Boulogne, F., 2020. Roughness-Induced Friction on Liquid Foams. Phys. Rev. Lett. 124, 118003. https://doi.org/10.1103/PhysRevLett.124.118003

Messelmi, F., 2019. On the blocking limit of steady-state flow of Herschel–Bulkley fluid. Math. Mech. Complex Syst. 7, 63–73. https://doi.org/10.2140/memocs.2019.7.63

Mierzejewska, S., Masłowska, S., Piepiórka-Stepuk, J., 2014. Evaluation of the efficiency of removing protein deposits from various surfaces by foam cleaning. Agric. Eng. 131–137. https://doi.org/10.14654/ir.2014.149.014

Moreno, E., Larese, A., Cervera, M., 2016. Modelling of Bingham and Herschel–Bulkley flows with mixed P1/P1 finite elements stabilized with orthogonal subgrid scale. J. Non-Newton. Fluid Mech. 228, 1–16. https://doi.org/10.1016/j.jnnfm.2015.12.005

Panckow, R.P., McHardy, C., Rudolph, A., Muthig, M., Kostova, J., Wegener, M., Rauh, C., 2021. Characterization of fast-growing foams in bottling processes by endoscopic imaging and convolutional neural networks. J. Food Eng. 289, 110151. https://doi.org/10.1016/j.jfoodeng.2020.110151

Parikh, D., Wu, Y., Peterson, C., Jarriel, S., Mooney, M., Tilton, N., 2019. The coupled dynamics of foam generation and pipe flow. Int. J. Heat Fluid Flow 79, 108442. https://doi.org/10.1016/j.ijheatfluidflow.2019.108442

Pierre, J., Leroy, V., 2016. ACOUSTICAL PROPERTIES OF LIQUID FOAMS 2.

Schad, T., Preisig, N., Blunk, D., Piening, H., Drenckhan, W., Stubenrauch, C., 2021. Less is more: Unstable foams clean better than stable foams. J. Colloid Interface Sci. 590, 311–320. https://doi.org/10.1016/j.jcis.2021.01.048

Schramm, L.L. (Ed.), 2000. Surfactants: fundamentals and applications in the petroleum industry. Cambridge University Press, Cambridge, U.K. ; New York.

Sherif, T., Ahmed, R., Shah, S., Amani, M., 2015. Rheological behavior of oil-based drilling foams. J. Nat. Gas Sci. Eng. 26, 873–882. https://doi.org/10.1016/j.jngse.2015.07.022

Stevenson, P. (Ed.), 2012. Front Matter, in: Foam Engineering. John Wiley & Sons, Ltd, Chichester, UK, pp. i–xv. https://doi.org/10.1002/9781119954620.fmatter

Sullivan, E., Yee, J., 1984. The viscosity of a foam (air in water emulsion) 6.

Tandiroglu, A., 2006. Effect of flow geometry parameters on transient heat transfer for turbulent flow in a circular tube with baffle inserts. Int. J. Heat Mass Transf. 49, 1559–1567. https://doi.org/10.1016/j.ijheatmasstransfer.2006.01.018

Tisné, P., Aloui, F., Doubliez, L., 2003. Analysis of wall shear stress in wet foam flows using the electrochemical method. Int. J. Multiph. Flow 29, 841–854. https://doi.org/10.1016/S0301-9322(03)00038-7

Tisné, P., Doubliez, L., Aloui, F., 2004. Determination of the slip layer thickness for a wet foam flow. Colloids Surf. Physicochem. Eng. Asp. 246, 21–29. https://doi.org/10.1016/j.colsurfa.2004.07.014

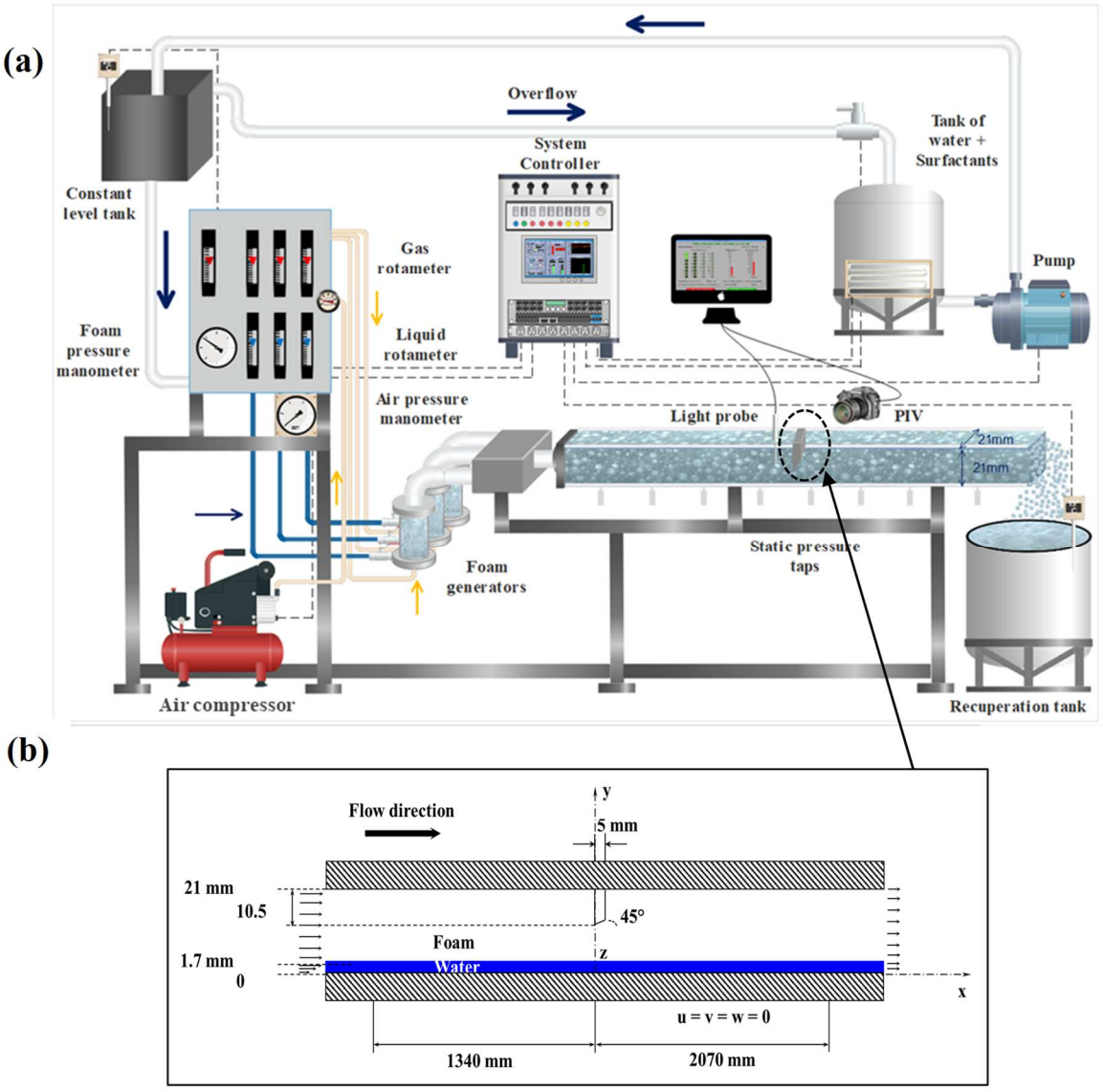

Figure. 1. Experimental set-up. **(a):** Design of the device. **(b):** Dimension of the pipe zone studied.

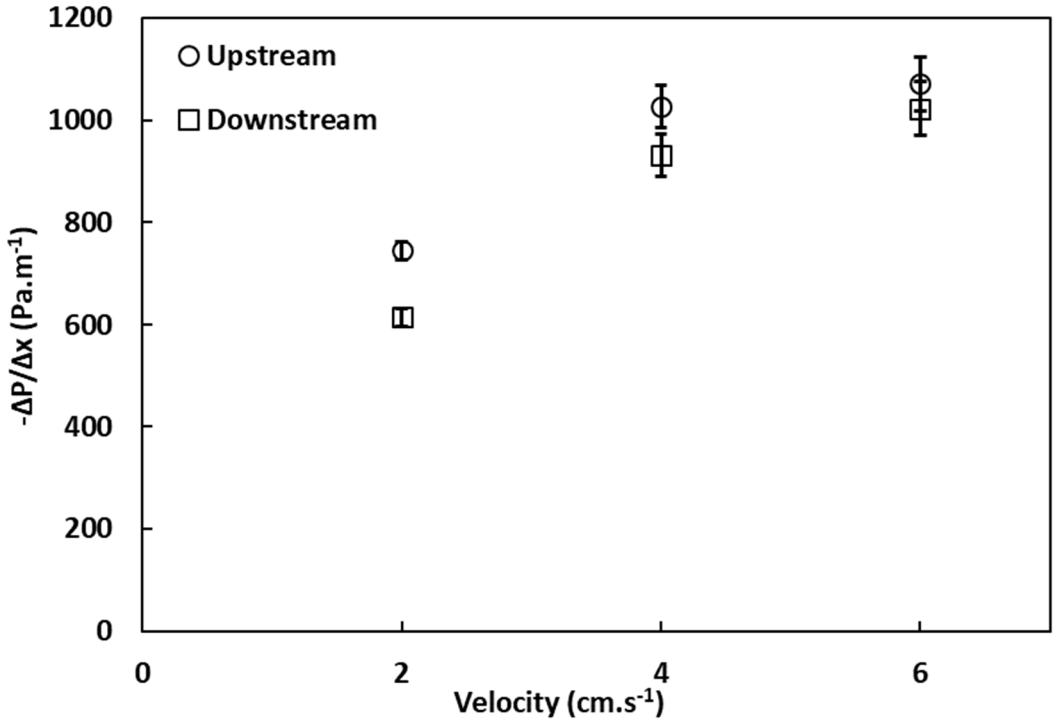

Figure. 2. Longitudinal pressure gradient upstream and downstream the fence.

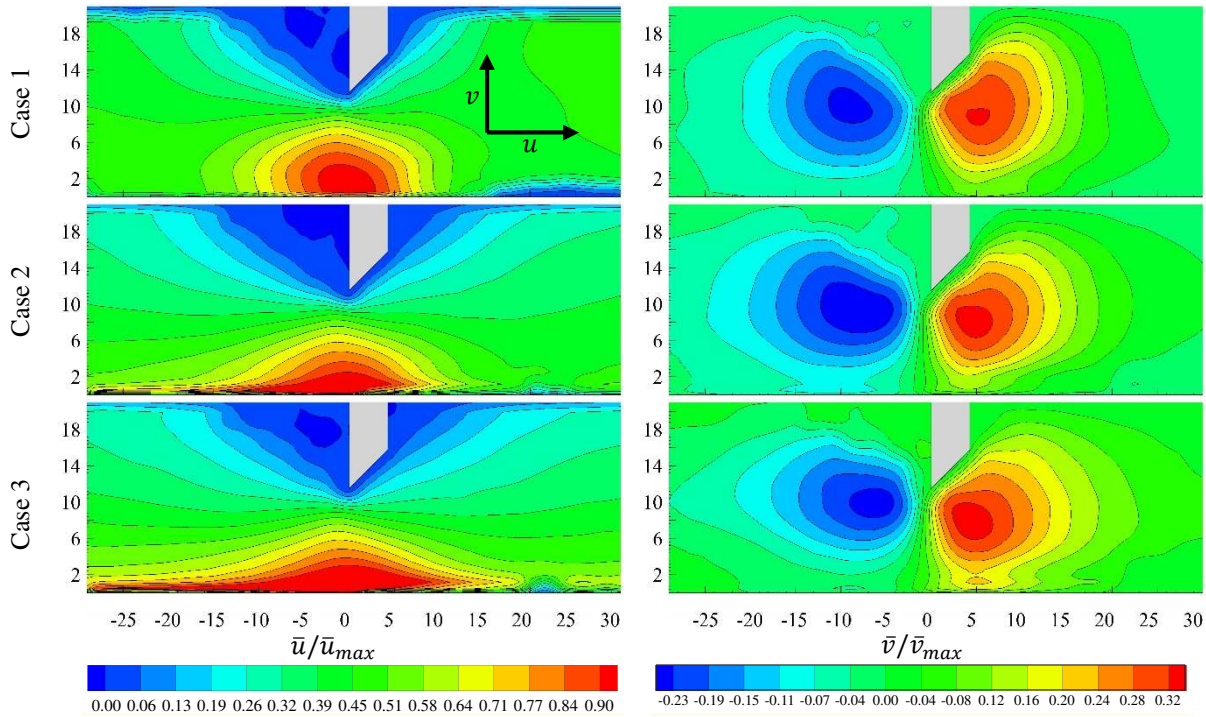

Figure. 3. Averaged axial $\bar{u}$, and vertical ($\bar{v}$) mean velocity components' fields for all cases under the fence.

Velocity measurements were obtained using the PIV technique. $\bar{u}_{max}$ was 4.3, 9, and 14 cm.s^{-1} and $\bar{v}_{max}$ was 1.3, 2.2, and 2.4 cm.s^{-1} for cases 1,2 and 3 respectively.

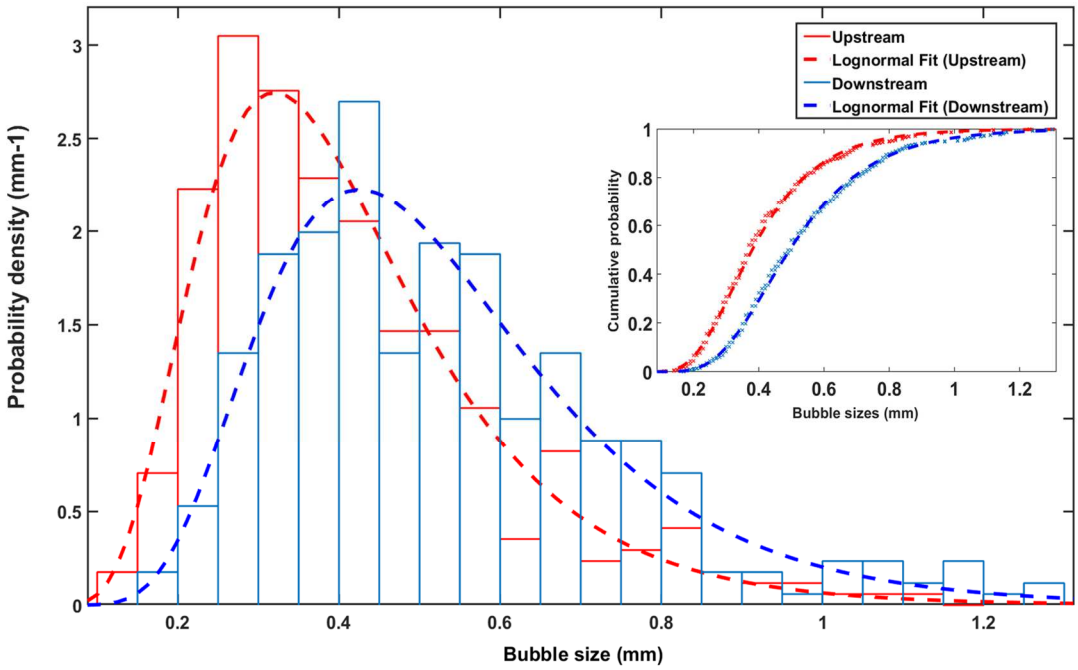

Figure. 4. Experimental example of the bubble size distribution for the case of foam at Re = 32. Density and cumulative probability of the bubble size upstream and downstream of the fence.

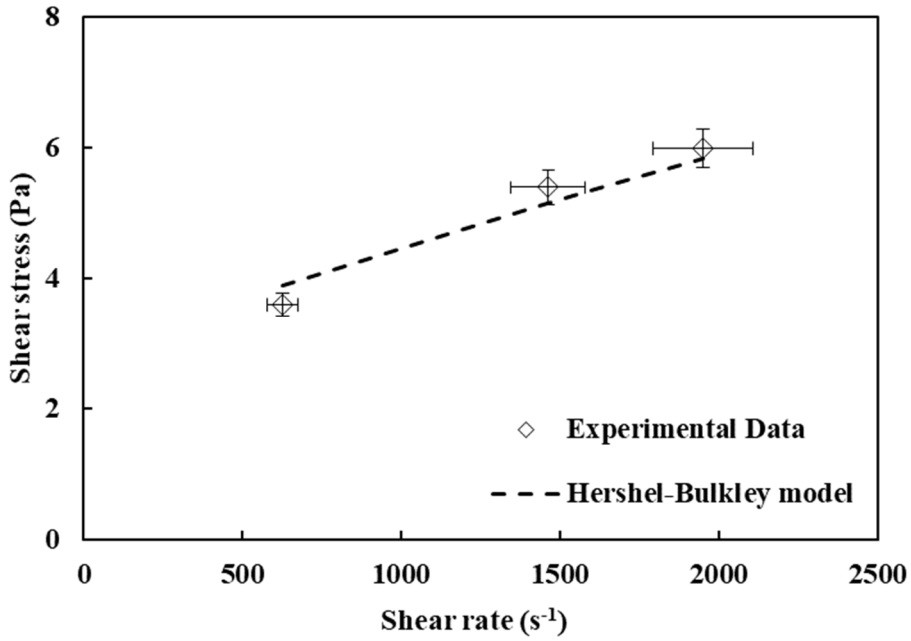

Figure. 5. Experimental flow curve of the wet foam studied.

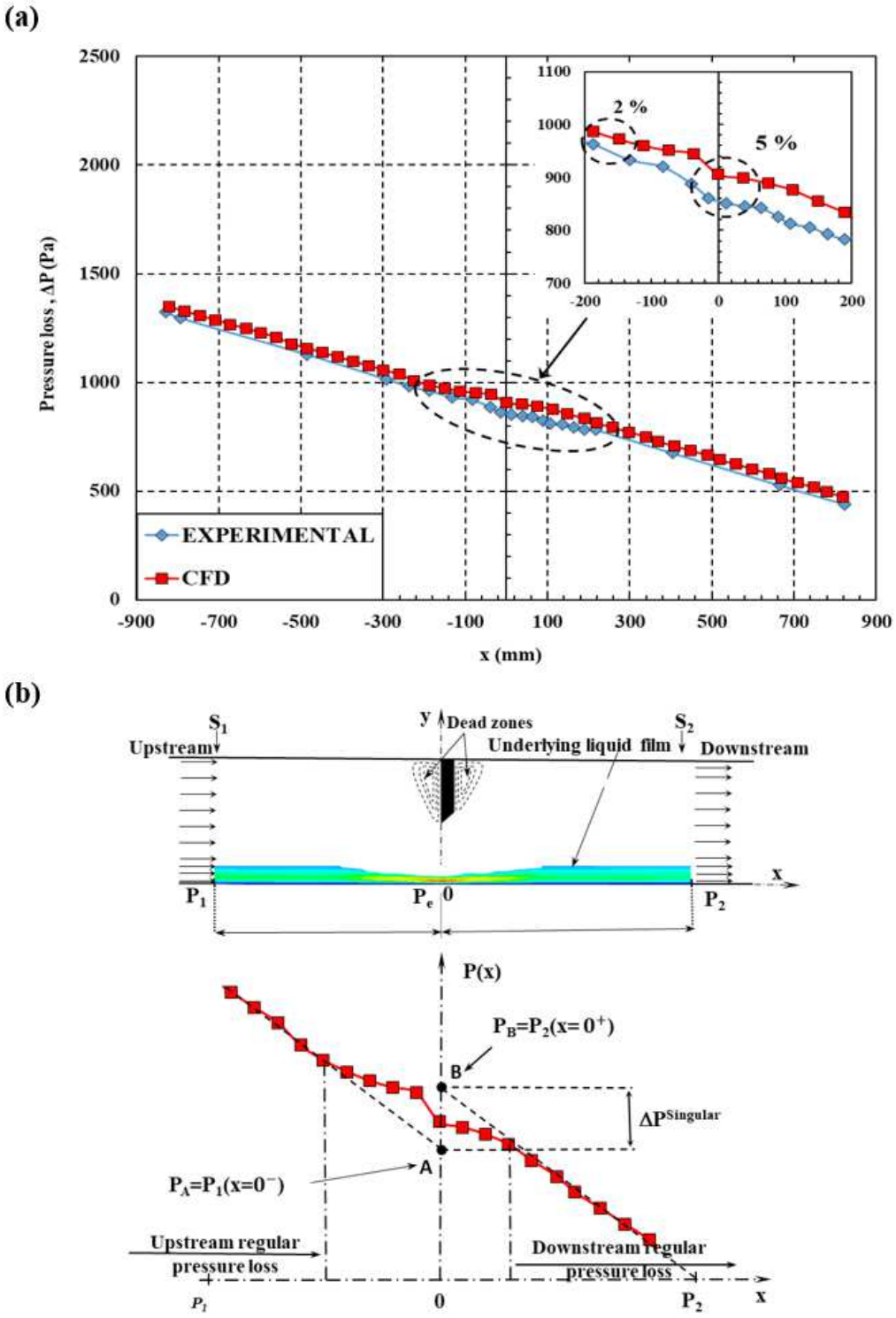

Figure. 6. Longitudinal static pressure drop of the foam flow at Re = 32. **(a):** Evolution of the longitudinal static pressure drop along the test channel. **(b):** Zoom on the area influenced by the fence.

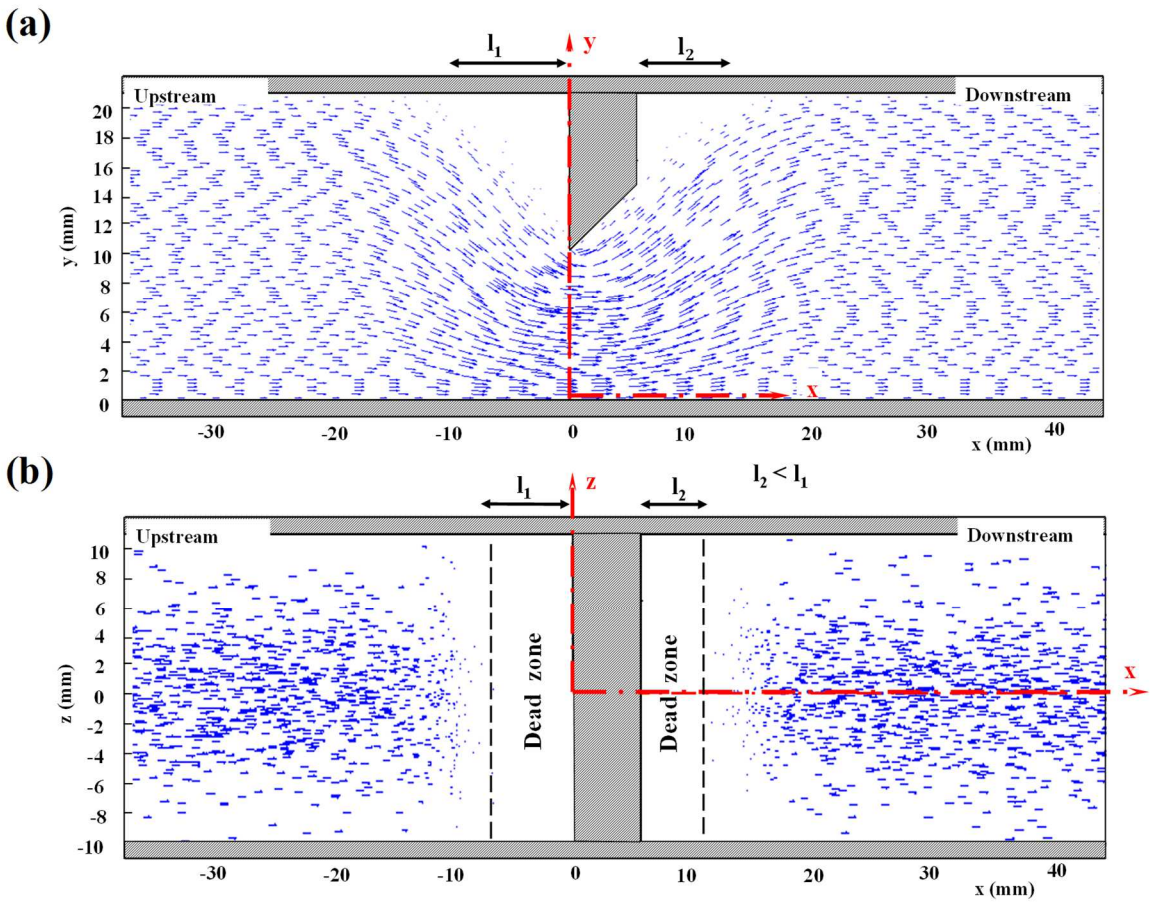

Figure. 7. Example of velocity field obtained under the fence at the middle axis of the duct by CFD simulation using the Herschel-Bulkley model (foam at Re = 32). **(a):** Lateral view. **(b):** Top view at y =19 mm.

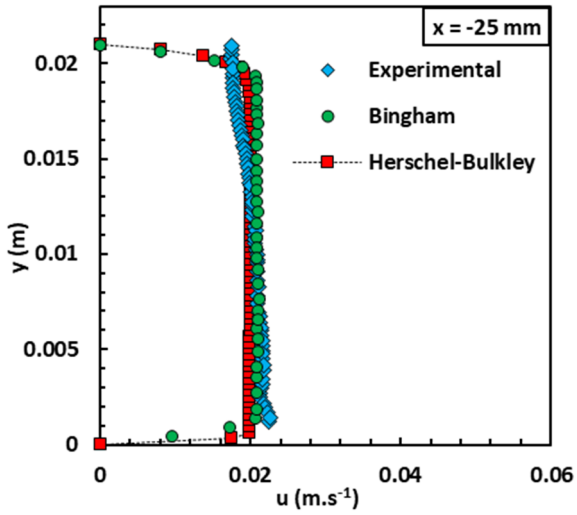
x = -25 mm
Experimental
Bingham
Herschel-Bulkley
y (m)
u (m.s-1)
0
0.005
0.01
0.015
0.02
0.04
0.06

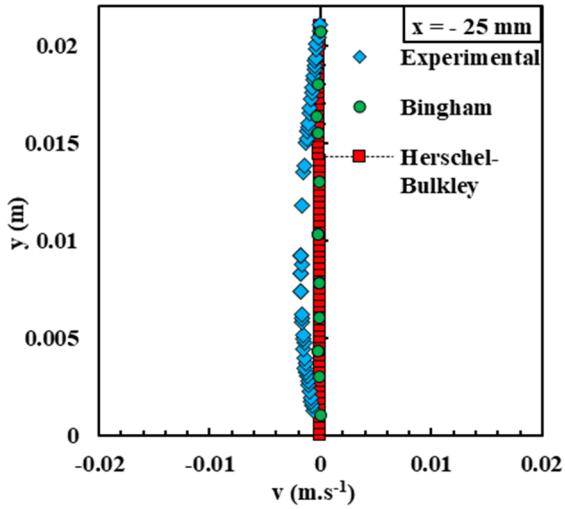
x = - 25 mm
Experimental
Bingham
Herschel-Bulkley
y (m)
v (m.s-1)
-0.02
-0.01
0.01
0.02

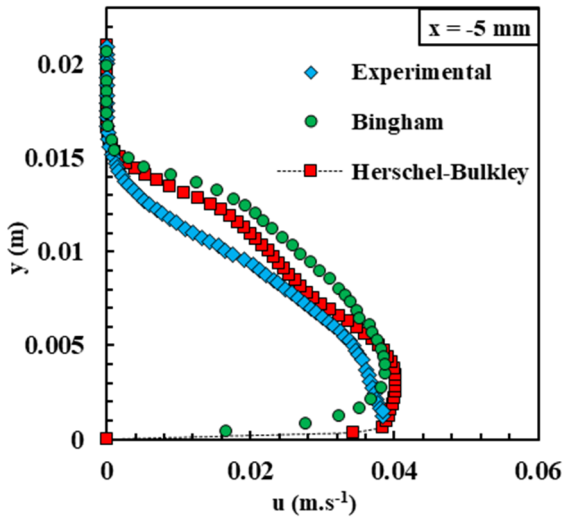
x = -5 mm
Experimental
Bingham
Herschel-Bulkley
y (m)
u (m.s-1)

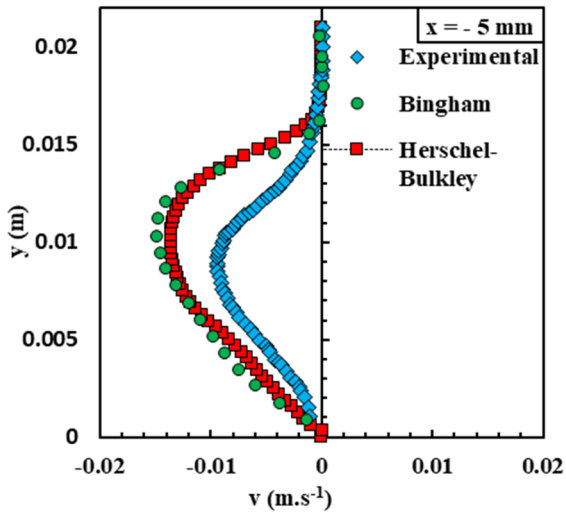
x = - 5 mm
Experimental
Bingham
Herschel-Bulkley
y (m)
v (m.s-1)

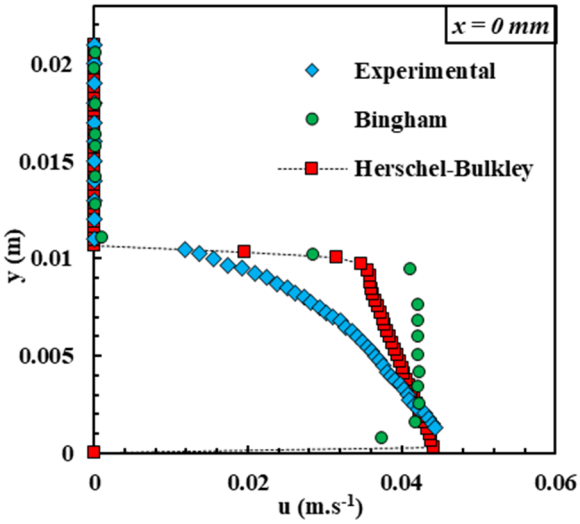
x = 0 mm
Experimental
Bingham
Herschel-Bulkley
y (m)
u (m.s-1)

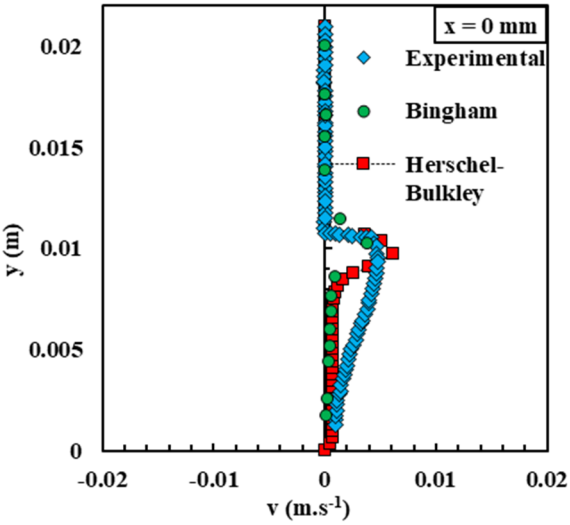
x = 0 mm
Experimental
Bingham
Herschel-Bulkley
y (m)
v (m.s-1)

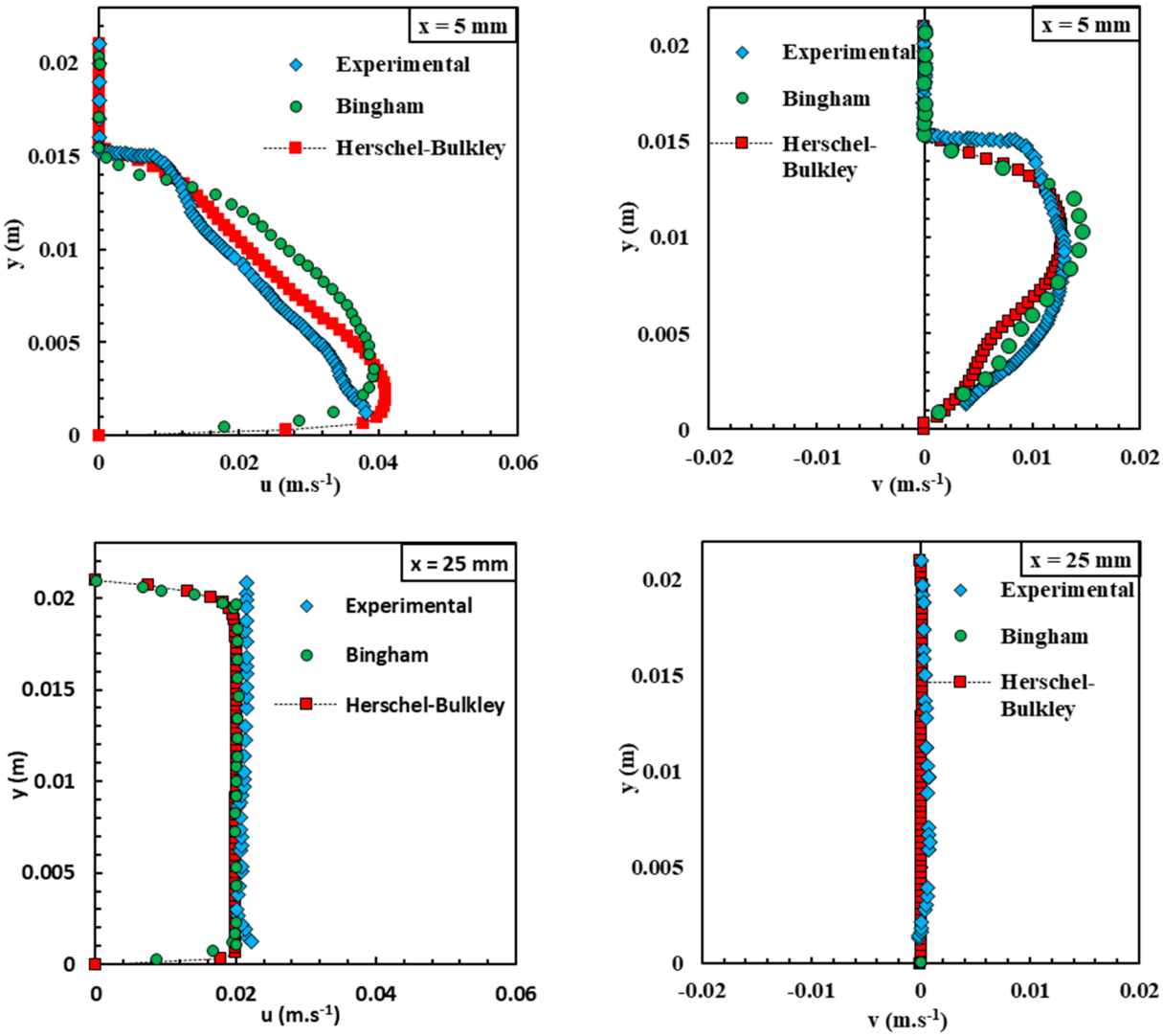

Figure. 8. Lateral averaged axial (u) and vertical (v) mean component velocity profiles for different positions near the singularity, for the case of foam at Re of 32.

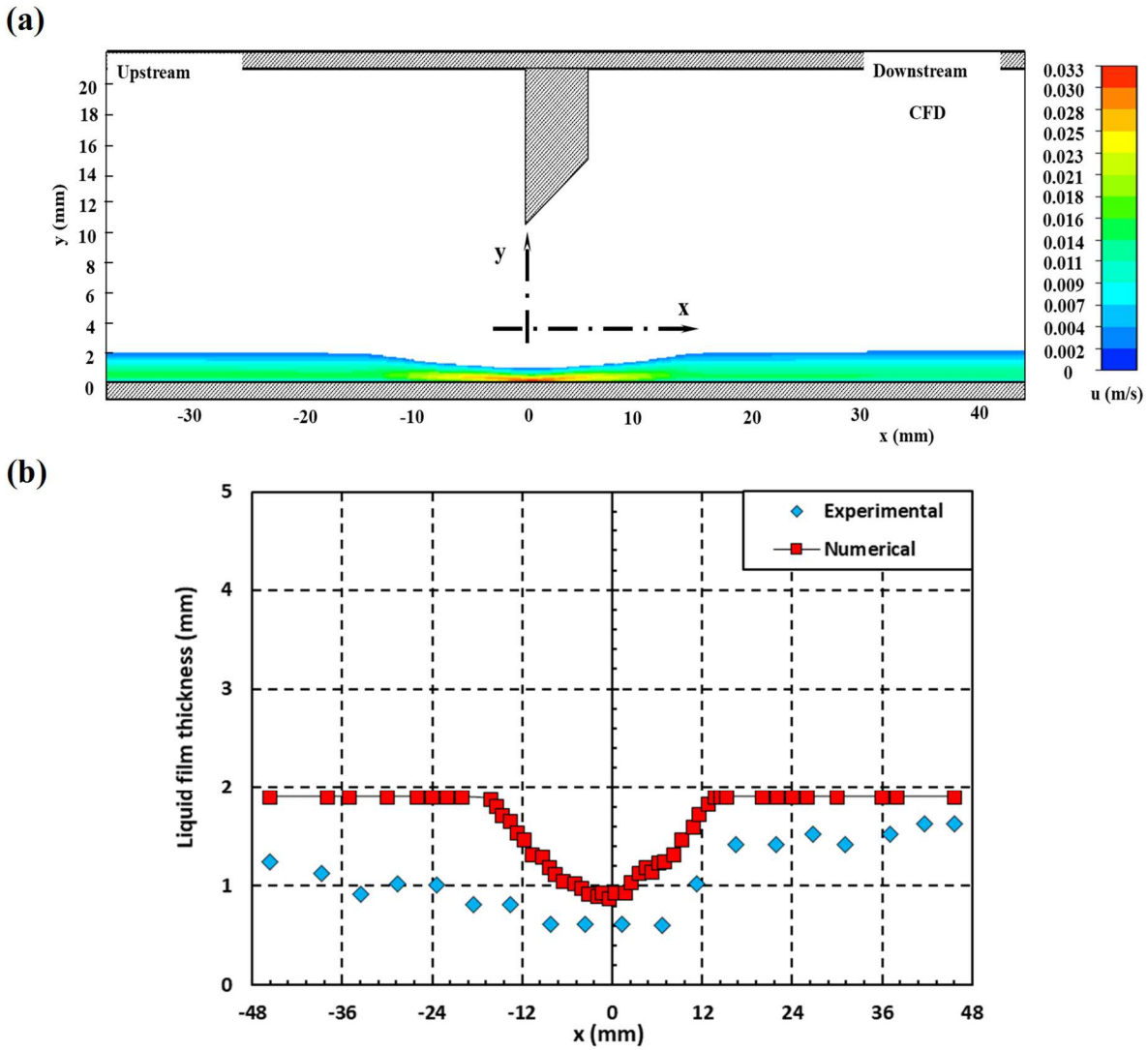

Figure. 9. Underlying liquid film located at the bottom of the horizontal duct. **(a):** Averaged axial velocity field. **(b):** Comparison of experimental (blue diamonds) and numerical simulation (red squares) underlying liquid film thickness. The foam in this simulation was defined by Hershel-Bulkley model.

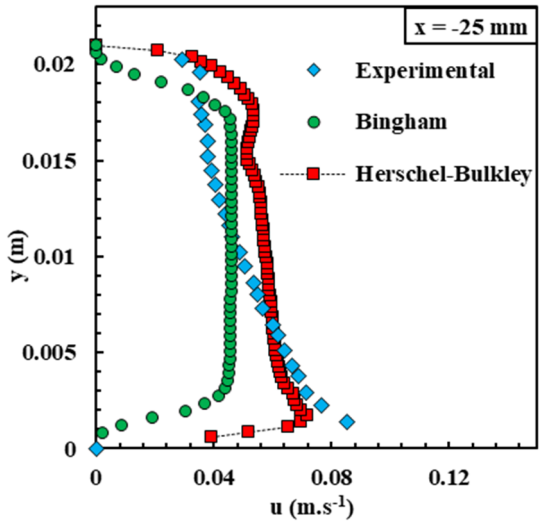
x = -25 mm
Experimental
Bingham
Herschel-Bulkley
y (m)
u (m.s-1)
0
0.005
0.01
0.015
0.02
0.04
0.08
0.12

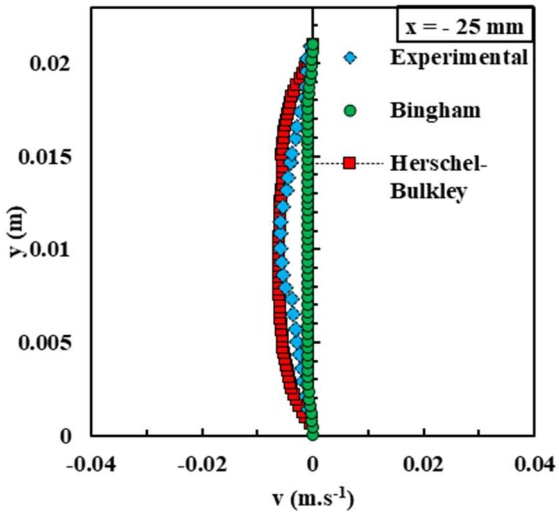
x = - 25 mm
Experimental
Bingham
Herschel-Bulkley
y (m)
v (m.s-1)
0
0.005
0.01
0.015
0.02
-0.04
-0.02
0.02
0.04

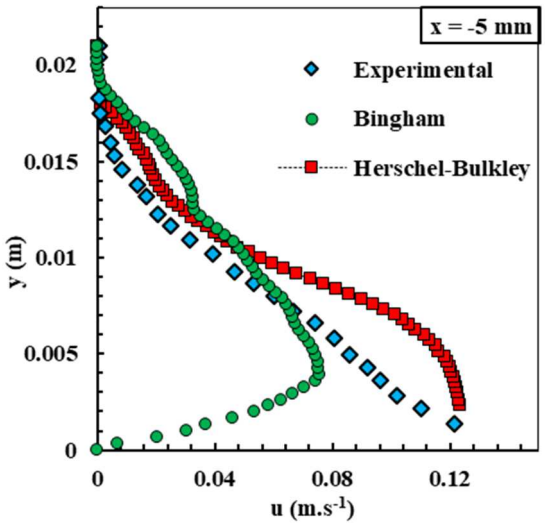
x = -5 mm
Experimental
Bingham
Herschel-Bulkley
y (m)
u (m.s-1)
0
0.005
0.01
0.015
0.02
0.04
0.08
0.12

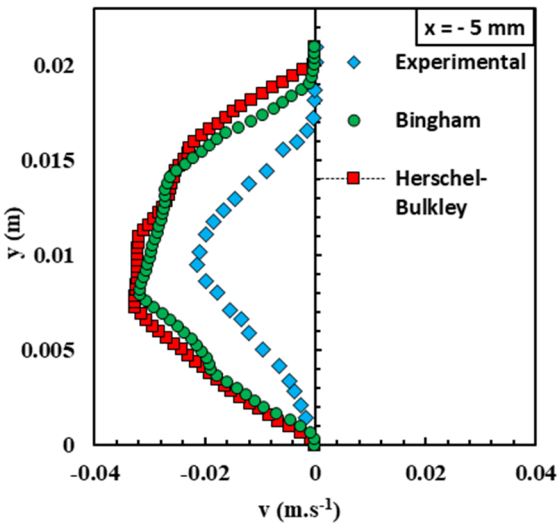
x = - 5 mm
Experimental
Bingham
Herschel-Bulkley
y (m)
v (m.s-1)
0
0.005
0.01
0.015
0.02
-0.04
-0.02
0.02
0.04

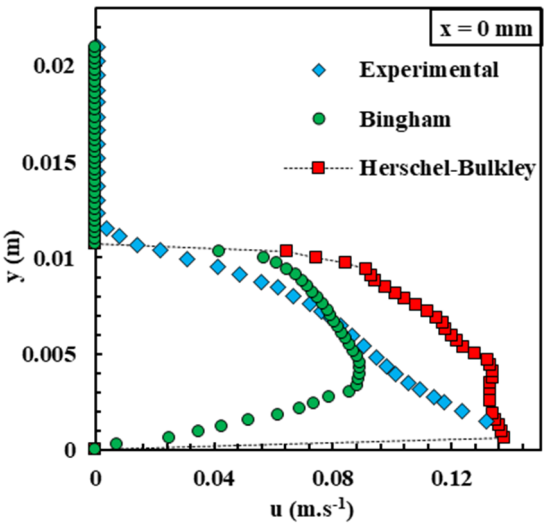
x = 0 mm
Experimental
Bingham
Herschel-Bulkley
y (m)
u (m.s-1)
0
0.005
0.01
0.015
0.02
0.04
0.08
0.12

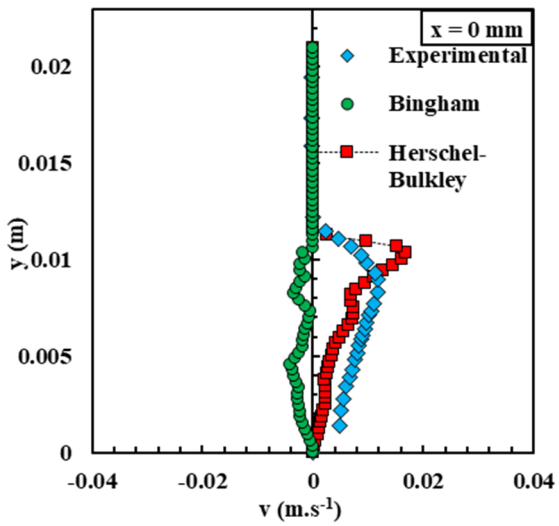
x = 0 mm
Experimental
Bingham
Herschel-Bulkley
y (m)
v (m.s-1)
0
0.005
0.01
0.015
0.02
-0.04
-0.02
0.02
0.04

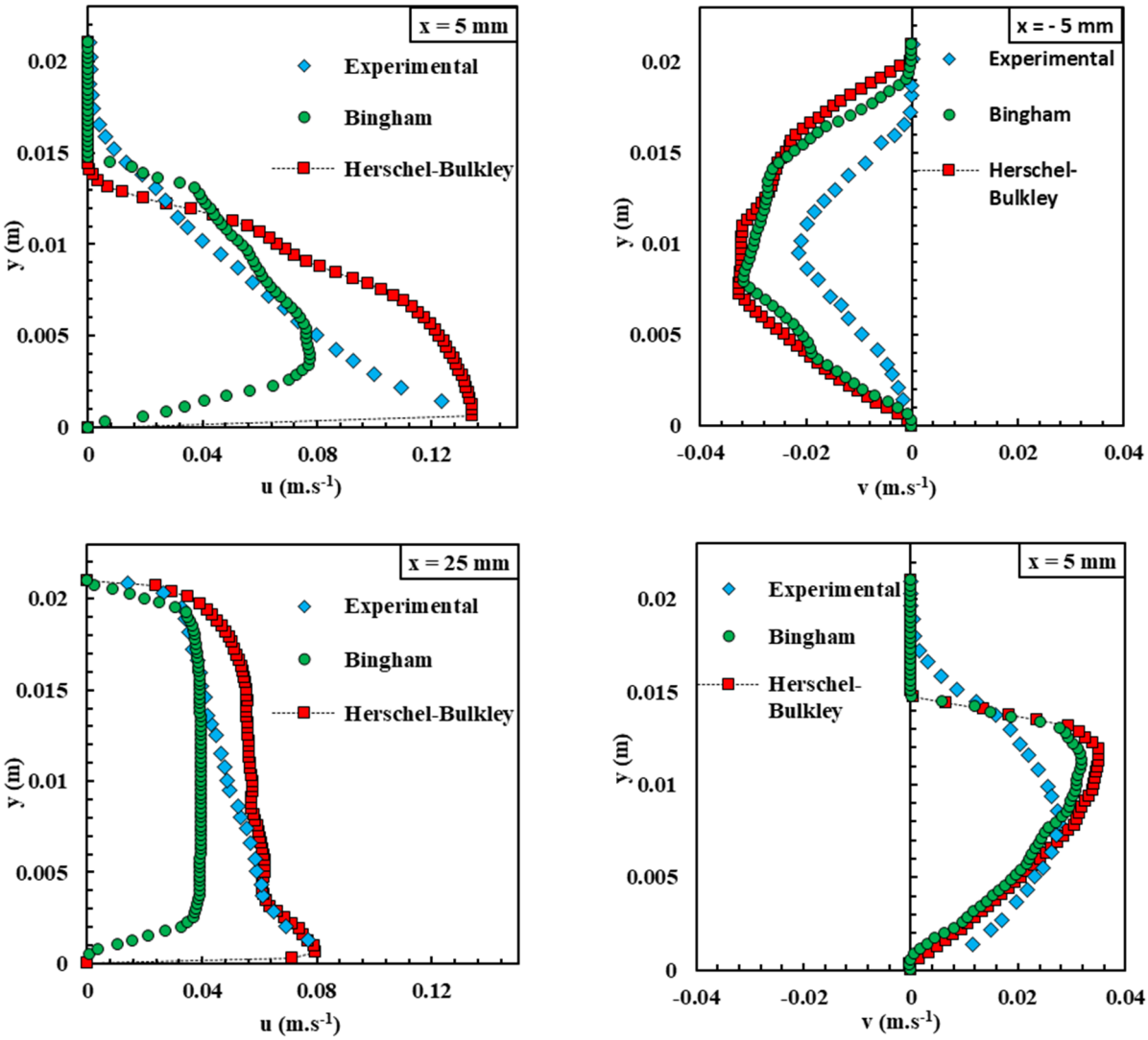

Figure. 10. Lateral averaged axial (u) and vertical (v) mean component velocity profiles for different positions near the singularity, for the case of foam at Re = 97 and different rheological models.

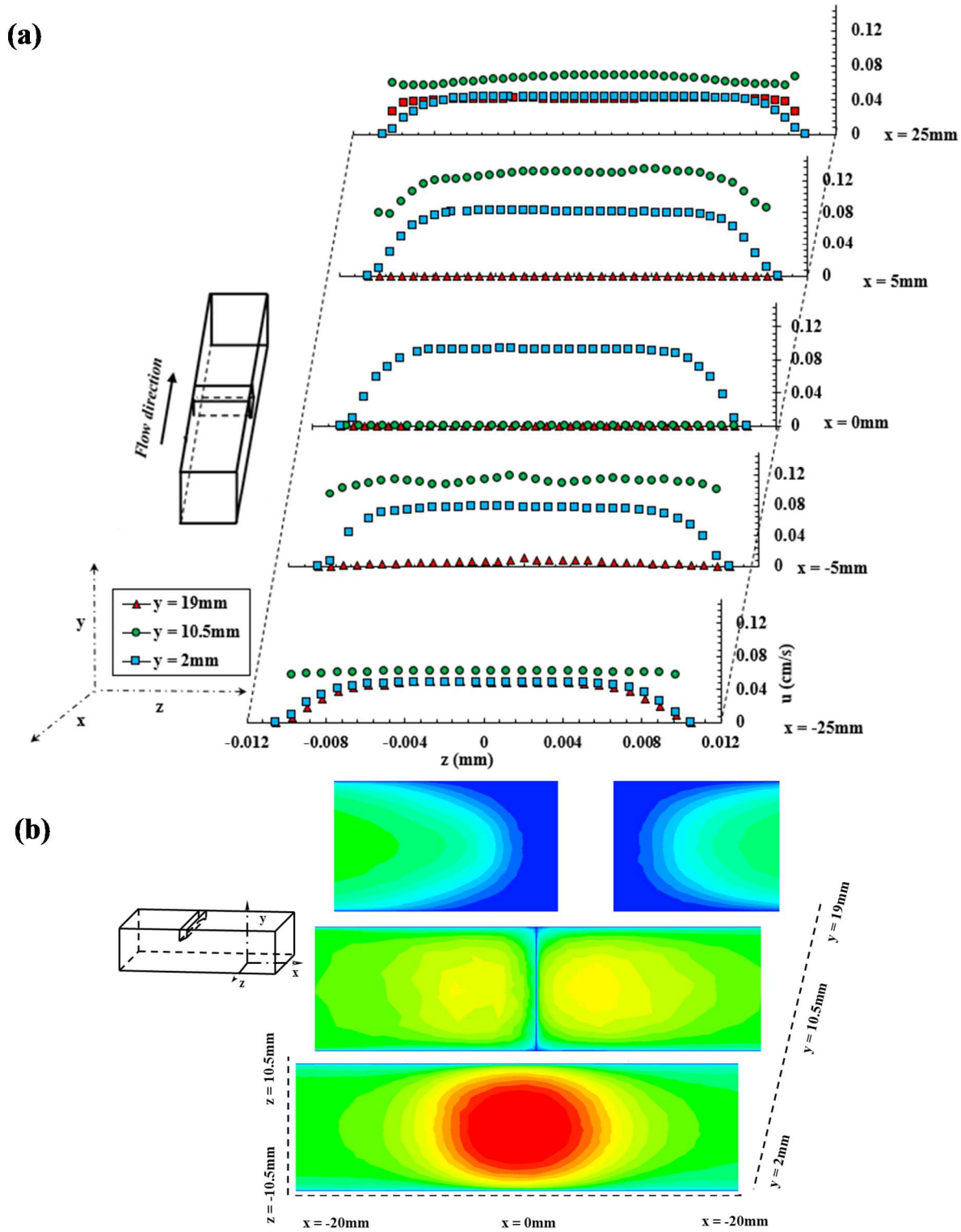

Figure. 11. CFD spanwise (top side) axial velocity at different locations in the vicinity of the singularity for case of foam at Re = 97. **(a):** averaged axial velocity component profiles. **(b):** Axial velocity component distribution for three horizontal planes located at: y = 2, 10.5, and 19 mm.

Table 1. Foam flow conditions at temperature of 20°C.

Flow Regime	Density ($kg.m^{-3}$)	Viscosity (mPa.s)	Mean velocity ($cm.s^{-1}$)	Reynolds number
Case 1: 1D	349.7	4.6	2	32
Case 2: 2D			4	65
Case 3: 3D			6	97

Table 2. Parameters of the two rheological models used. The parameters of the Herschel-Bulkley (CFD) model derived from the experimental flow curve (experimental, 20°C) were thus refined to obtain the best match between the CFD results and the experimental data.

Model	Yield Stress τ_0 (Pa)	Consistency k (Pa.s)	index n	Density ρ (kg.m^{-3})
Hershel-Bulkley (experimental; 20°C)	2.7	0.005	0.85	350
Bingham (CFD)	6.4	0.001	1	350
Hershel-Bulkley (CFD)	3.9	0.0015	0.80	350